

The initial conditions of isolated star formation. V: ISOPHOT imaging and the temperatures and energy balance of pre-stellar cores

D. Ward-Thompson¹, P. André² & J. M. Kirk¹

¹*Department of Physics & Astronomy, Cardiff University, PO Box 913, 5 The Parade, Cardiff CF2 3YB*

²*CEA, DSM, DAPNIA, Service d'Astrophysique, C.E. Saclay, F-91191 Gif-sur-Yvette Cedex, France*

Accepted 2001 September 7; received 2001 August 7; in original form 2000 December 21.

ABSTRACT

ISO data taken with the long-wavelength imaging photo-polarimeter ISOPHOT are presented of 18 pre-stellar cores at three far-infrared wavelengths – 90, 170 & 200 μm . Most of the cores are detected clearly at 170 and 200 μm , but only one is detected strongly at 90 μm , indicating that mostly they are very cold, with typical temperatures of only ~ 10 – 20 K. Colour temperature images are constructed for each of the cores. Most of the cores are seen to be either isothermal, or to have associated temperature gradients from the core centres to their edges, with all except one being cooler at the centre. We compare the data with previous ISOCAM absorption data and calculate the energy balance for those cores in common between the two samples. We find that the energy radiated by each core in the far-IR is similar to that absorbed at shorter wavelengths. Hence there is no evidence for a central heating source in any of the cores – even those for which previous evidence for core contraction exists. This is all consistent with external heating of the cores by the local interstellar radiation field, confirming their pre-stellar nature.

Key words: stars: formation – ISM: dust

1 INTRODUCTION

The process of star formation is currently only partially understood. One of the main problems is that we do not know the initial conditions which pertain in the clouds from which stars form. The initial form of the radial variation of density, temperature, velocity and magnetic field are crucial to the protostellar collapse phase of star formation. This gap in our knowledge is currently one the major limiting factors in our ability to understand the star formation process for relatively low-mass stars (0.2 – $2 M_{\odot}$).

The main protostellar collapse phase was identified observationally by André, Ward-Thompson & Barsony (1993 – hereafter AWB93), and labelled the Class 0 stage. The subsequent Class I stage (Lada & Wilking 1984; Lada 1987) represents the late accretion phase during which the remnant circumstellar envelope accretes onto the central protostar and disk (André 1994; 1997; Ward-Thompson 1996). The final pre-main-sequence stages of Classes II & III (Lada & Wilking 1984; Lada 1987) correspond to the Classical T Tauri (CTT) and Weak-line T Tauri (WTT) stages respectively (André & Montmerle 1994).

These protostellar and pre-main-sequence stages are understood at least in outline (for a review, see: André, Ward-

Thompson & Barsony 2000 – hereafter AWB00). Infall has been reported in Class 0 sources by a number of authors (e.g. Zhou et al. 1993; Ward-Thompson et al. 1996). However, the manner of the collapse remains a matter for debate. The old ideas of inside-out collapse (e.g. Shu et al. 1987) have been disputed by many authors (e.g. Foster & Chevalier 1993; Whitworth et al. 1996), and recently appear to have been finally disproved observationally (Tafalla et al. 1998). Broad general agreement now appears to be emerging that the collapse occurs at a non-constant rate, which decreases with time throughout the accretion phase (e.g. Kenyon & Hartmann 1995; Henriksen, André & Bontemps 1997; Safier, McKee & Stahler 1997).

However, the exact form of the collapse depends almost entirely on the initial conditions (Whitworth & Summers 1985; Foster & Chevalier 1993; Whitworth et al. 1996). A decreasing accretion rate is obtained when the initial radial density is relatively flat in the centre, and steepens towards the edge (Foster & Chevalier 1993; Henriksen et al 1997; Whitworth & Ward-Thompson 2001).

In this series of papers we are exploring observationally the initial conditions for star formation in order to determine empirically the physical parameters in molecular cloud cores which are on the verge of forming stars. We selected

arXiv:astro-ph/0109173v1 11 Sep 2001

Table 1. Source positions, observing details and raw flux densities. In this table, and in all subsequent figures and tables, the sources are listed in increasing order of Right Ascension. The positions quoted are the 200- μm peak positions. In all cases the 170- μm peak positions agree to within the telescope resolution. The target dedicated time (TDT) designation of each observation is listed (see text). The 170- & 200- μm observations have the same TDT as they were observed together. The 90- μm observations were taken at a different time. The peak flux densities are quoted in MJy/sr, and the total flux densities are quoted in Jy, to an accuracy of 3 significant figures. The absolute calibration errors are $\sim \pm 30\%$ (see text for discussion). Note that these flux densities have not had any background removal, so they include flux from the core, the extended cloud and other backgrounds (including Zodiacal). The 90- μm peak upper limit quoted in each case is simply the value at the brightest point, which may not be exactly coincident with the source, and also includes extended cloud emission. This is shown as an upper limit in all cases except L1689A (which has a detection) and L1517C (which has no data).

Source Name	R.A. (2000)	Dec. (2000)	TDT 90 μm	TDT 170/200 μm	Peak flux densities (MJy/sr)			Total flux densities in mapped areas (Jy)		
					90 μm	170 μm	200 μm	90 μm	170 μm	200 μm
L1498	04 ^h 10 ^m 52.2 ^s	+25° 09' 12''	65400701	67900714	≤ 21.0	73.9	81.7	146	707	714
L1517C	04 ^h 54 ^m 45.3 ^s	+30° 35' 46''	–	68600815	–	84.6	78.3	–	840	859
L1517A	04 ^h 55 ^m 11.7 ^s	+30° 33' 14''	68001003	68600716	≤ 28.9	88.6	91.1	195	874	862
L1517B	04 ^h 55 ^m 16.7 ^s	+30° 37' 08''	68601413	68200926	≤ 26.7	77.4	90.5	177	886	956
L1512	05 ^h 04 ^m 07.6 ^s	+32° 44' 24''	65200804	65200717	≤ 29.6	81.9	93.2	181	798	815
L1544	05 ^h 04 ^m 17.4 ^s	+25° 11' 29''	68601205	68600618	≤ 32.7	104	116	219	986	975
L1582A	05 ^h 32 ^m 00.0 ^s	+12° 31' 47''	69201506	69201419	≤ 102	315	374	463	2280	2550
L183	15 ^h 54 ^m 12.5 ^s	–02° 52' 04''	62701701	62701813	≤ 18.3	76.2	77.2	107	501	475
L1696A	16 ^h 28 ^m 32.7 ^s	–24° 18' 14''	12002302	12002214	≤ 191	308	368	1050	2120	2610
L1709A	16 ^h 30 ^m 48.6 ^s	–23° 41' 34''	12001407	12001619	≤ 122	185	229	605	1340	1580
L1689A	16 ^h 32 ^m 14.3 ^s	–25° 03' 29''	11800703	11800415	252	649	701	1240	3380	4060
L1709C	16 ^h 33 ^m 57.8 ^s	–23° 40' 33''	12002408	12001520	≤ 89.5	179	224	445	1090	1440
L1689B	16 ^h 34 ^m 46.2 ^s	–24° 37' 46''	12001904	11800516	≤ 138	260	235	697	1630	1450
L204B	16 ^h 47 ^m 39.1 ^s	–11° 58' 02''	11400309	11400421	≤ 60.0	145	191	329	1020	1220
L63	16 ^h 50 ^m 16.0 ^s	–18° 04' 40''	11800605	11800317	≤ 54.5	120	131	290	709	656
B68	17 ^h 22 ^m 37.9 ^s	–23° 50' 24''	11800910	11800822	≤ 65.4	109	148	316	657	918
B133	19 ^h 06 ^m 11.6 ^s	–06° 53' 03''	11402306	12001318	≤ 58.5	134	184	285	747	980
L1155C	20 ^h 43 ^m 13.0 ^s	+67° 52' 00''	12000212	12000324	≤ 22.8	71.2	75.6	116	442	419

for study the regions which were identified by Myers and co-workers (e.g. Myers & Benson 1983; Myers, Linke & Benson 1983; Benson & Myers 1989) from the catalogues of Lynds and others (e.g. Lynds 1962), and which were observed in various transitions of NH_3 , CO and other molecules (Benson & Myers 1989 and references therein). But we selected from these a sub-sample of cores which do not contain IRAS (Infra-Red Astronomical Satellite) sources (Beichman et al. 1986; 1988), on the grounds that these should be at an earlier evolutionary stage, with the cores with IRAS sources having already formed protostars at their centres.

In Paper I (Ward-Thompson et al. 1994) we coined the term pre-protostellar cores to refer to those cores without embedded stars (the ‘starless cores’ of Myers and co-workers) which appeared to be sufficiently centrally condensed to be about to form stars. We have subsequently shortened this term to pre-stellar cores (c.f. AWB93). Paper I discussed the results of a submillimetre study of some pre-stellar cores, and found that the cores all appeared to follow a similar form of density profile to that predicted by theory to produce a decreasing accretion rate with time (Foster & Chevalier 1993).

In Papers II & III (André, Ward-Thompson & Motte 1996; Ward-Thompson, Motte & André 1999) we presented studies at 1.3-millimetre wavelength of a number of pre-stellar cores, and compared the findings in detail with models which predict evolution of molecular cloud cores by ambipolar diffusion (e.g. Basu & Mouschovias 1995). It was found that, although the radial density profiles of the cores appear similar to those predicted by ambipolar diffusion

models, the details of the time-scales required by the models at different stages did not appear to match the life-times we calculated from the numbers we detected at each evolutionary stage. However, these results were based on relatively small number statistics, so we intend to improve the accuracy of the results by enlarging our statistical sample.

In Paper IV (Jessop & Ward-Thompson 2001) we carried out a detailed spectroscopic study of one of the cores, and showed that a temperature gradient from the outside-in was required to explain the data. If this is true for all of the cores, then this will affect any density gradient measurements inferred from submillimetre and millimetre data. Therefore, it appears necessary to explore such temperature gradient effects in a wide sample of cores using infra-red wavelengths.

One of the difficulties associated with studying pre-stellar cores is that they have not previously been detected in the infra-red, either from the ground, or by the IRAS satellite out to 100 μm – this is one of the selection criteria of these sources. However, Papers I–III have shown us that the spectral energy distributions increase with decreasing wavelength from 1.3 mm to 350 μm . Consequently the spectra must peak between 100 and 350 μm . So we decided to observe the pre-stellar cores with the Infrared Space Observatory (ISO) at far-infrared wavelengths from 90 to 200 μm using the long wavelength imaging photo-polarimeter instrument ISOPHOT (see Ward-Thompson et al. 1998 for preliminary results). In this paper we present the complete results of our ISOPHOT study of pre-stellar cores.

Table 2. Source background level estimates (including Zodiacal background) in MJy/sr quoted to 3 significant figures. B1 represents the lowest background emission level in each region. B2 is the level of emission in the extended cloud, not associated with the pre-stellar core. For L1517A, B & C a common B2 area was taken. The quoted errors are the 1σ variations in each background region. Absolute calibration errors are $\pm 30\%$ (see text for details).

Source Name	Background level – B1 (MJy/sr)			Background level – B2 (MJy/sr)		
	90 μ m	170 μ m	200 μ m	90 μ m	170 μ m	200 μ m
L1498	17.2 \pm 0.9	39.5 \pm 2.5	43.4 \pm 1.4	20.3 \pm 0.2	67.2 \pm 0.4	67.8 \pm 0.7
L1517C	–	60.0 \pm 0.7	55.7 \pm 0.9	–	69.0 \pm 2.1	71.4 \pm 2.3
L1517A	22.2 \pm 7.3	59.4 \pm 1.4	53.7 \pm 1.4	25.0 \pm 5.3	69.0 \pm 2.1	71.4 \pm 2.3
L1517B	22.2 \pm 7.3	56.7 \pm 2.1	61.7 \pm 2.1	25.0 \pm 5.3	69.0 \pm 2.1	71.4 \pm 2.3
L1512	24.2 \pm 0.7	47.7 \pm 2.1	44.5 \pm 1.3	26.0 \pm 0.9	75.1 \pm 3.2	83.1 \pm 3.8
L1544	26.7 \pm 0.7	65.3 \pm 1.3	56.0 \pm 2.3	29.9 \pm 0.9	71.8 \pm 2.3	60.9 \pm 4.6
L1582A	45.0 \pm 2.3	72.4 \pm 14	81.5 \pm 15	74.5 \pm 3.4	200 \pm 5.7	206 \pm 6.7
L183	14.9 \pm 0.2	36.7 \pm 3.4	28.3 \pm 4.4	16.4 \pm 0.7	63.4 \pm 2.5	56.4 \pm 2.5
L1696A	135 \pm 4.8	216 \pm 5.5	252 \pm 11	178 \pm 2.5	270 \pm 5.0	336 \pm 5.5
L1709A	94.3 \pm 1.3	160 \pm 9.1	176 \pm 5.9	110 \pm 2.3	175 \pm 1.3	202 \pm 4.4
L1689A	154 \pm 8.0	280 \pm 15	373 \pm 14	212 \pm 10	376 \pm 12	465 \pm 17
L1709C	60.9 \pm 0.9	109 \pm 2.3	141 \pm 2.5	85.2 \pm 2.7	163 \pm 1.9	217 \pm 3.2
L1689B	108 \pm 2.5	173 \pm 3.2	140 \pm 4.4	117 \pm 1.3	213 \pm 5.5	192 \pm 2.7
L204B	50.6 \pm 0.9	100 \pm 3.9	107 \pm 6.1	55.0 \pm 6.5	127 \pm 3.8	138 \pm 11
L63	40.1 \pm 1.9	67.4 \pm 3.4	55.5 \pm 2.7	49.3 \pm 1.3	75.1 \pm 1.4	56.0 \pm 1.9
B68	47.0 \pm 1.9	67.2 \pm 1.1	98.9 \pm 1.1	58.7 \pm 1.1	85.4 \pm 1.1	114 \pm 2.1
B133	45.7 \pm 1.1	69.0 \pm 1.3	82.7 \pm 5.3	55.7 \pm 0.7	100 \pm 1.4	130 \pm 5.0
L1155C	16.7 \pm 0.7	40.5 \pm 1.1	32.2 \pm 0.9	19.0 \pm 0.7	53.7 \pm 5.7	46.6 \pm 6.5

2 OBSERVATIONS

The Infrared Space Observatory (ISO) was launched by the European Space Agency (ESA) on 1995 November 17 and began routine observations for the community on 1996 February 4. It finally ceased astronomical observations on 1998 April 8, almost a year longer than originally envisaged (Kessler et al., 1996). Our observations were carried out with the imaging photo-polarimeter ISOPHOT (Lemke et al., 1996) during a number of different orbits in the course of two different observing programmes.

Observations for the first programme, which was allocated time in the first call for observing proposals, took place predominantly during the period 1996 March 10–16 in orbits 114–120, and covered the sources in the R.A. range 16–20^h. The source L183, at an R.A. of 15^h, was observed during orbit 627 on 1997 August 4. The second programme, which was allocated time in the second call for observing proposals, took place during the period from 1997 August 29 to October 8 in orbits 652–692, and observed all of our sources in the R.A. range 04–05^h.

Table 1 lists our target sources. A total of 18 sources in 16 dark clouds were observed at each of the three wavelengths, 90, 170 & 200 μ m (except for the L1517C part of the L1517 cloud, which was not observed at 90 μ m due to time constraints). The total time taken for all of the observations was about 52,000 seconds. The target dedicated time (TDT) of every observation is listed in Table 1. The TDT is a unique 8-digit reference number for every observation that is stored in the ISO data archive (Arviset & Prusti 1999; Kessler et al., 2000). The first 3 digits of the TDT specify the orbit number in which the observations were taken and the remaining digits specify the observation number within that orbit. In each case the 170- & 200- μ m observations have the same TDT as they were observed together. Usually the 90- μ m observations were taken at a different time.

All of the observations were carried out using ISOPHOT in its over-sampled mapping mode – astronomical observation template (AOT) reference code PHT32. In this mode the source is mapped by using the chopper to position the source on the detector array at a series of positions, separated by less than the detector resolution, intermediate between successive spacecraft pointings. We used a chopper throw of 30 arcsec at the two longer wavelengths (C-200 and C-160 – see below) and 15 arcsec at the shorter wavelength (C-90 – see below) such that we were guaranteed a factor of at least 2 over-sampling at all wavelengths. A map was built up of a series of such scans in a raster fashion (for details, see: Klaas et al., 1994).

The filters used were the C-200 filter, which has a reference wavelength of 200 μ m and bandwidth full width at half maximum (FWHM) \sim 30 μ m, the C-160 filter, which actually has a peak wavelength of 170 μ m and bandwidth FWHM of \sim 50 μ m, and the C-90 filter, which has a peak wavelength of 90 μ m and FWHM \sim 40 μ m (Klaas et al. 1994). The C-200 and C-160 filters are associated with the PHT-C200 camera, which has four pixels in a 2 \times 2 array with each pixel 90 \times 90 arcsec square. The C-90 filter is associated with the PHT-C100 camera, which has nine pixels in a 3 \times 3 array with each pixel 45 \times 45 arcsec square (Klaas et al. 1994). Since all of the data were mapped in over-sampled mapping mode, it was decided to re-bin all data uniformly onto a grid of 45 \times 45 arcsec square pixels in Right Ascension and Declination. These data are reproduced in Figures 1–8 as isophotal contour maps superposed on grey-scale images.

The data were reduced using version 7 (V7) of the PHOT Interactive Analysis (PIA) software (Gabriel et al. 1997; Laureijs et al. 1998; 2001) in the standard way. This procedure takes into account instrumental effects such as detector responsivity and linearity, transient behaviour, dark current, detector saturation, bias, stray light and chopper vignetting (Laureijs et al. 2001).

Table 3. Source extended flux densities and full width at half maximum (FWHM) sizes. The FWHM are estimated from the 200- μm data using the ‘Best est.’ (see below) background subtraction (the differences at other wavelengths are insignificant). The columns headed ‘Best est.’ represent our best estimates of the background-subtracted flux densities of the pre-stellar cores measured within an aperture size equal to the FWHM sizes. For the 200- and 170- μm data: the columns headed B1 & B2 represent the flux densities in the FWHM using different methods for removing the background flux densities due to the general far-infrared background, and the extended cloud emission respectively (see text for discussion). The best estimate columns use a first-order polynomial background across the field, while B1 & B2 can be thought of as representing the full range of possible variation. The error-bars quoted are the residual errors from the background removal process, and these are generally dominated by fluctuations in this background. The absolute calibration errors are $\pm 30\%$. For the 90- μm data, upper limits are recorded for all sources, which are the 3σ variations in the background, except L1517C (which wasn’t observed at 90 μm) and L1689A (which was detected at 90 μm). Sources marked with a * are either marginal detections at 90 μm ($\leq 5\sigma$) or else contain a peak which is not coincident with the source at 170 and 200 μm . The 90- μm fluxes of these secondary peaks are: L1582A – $33\pm 3.8\text{Jy}$; L1709C – $15\pm 3.2\text{Jy}$; B68 – $6\pm 1.5\text{Jy}$; and B133 – $15\pm 5\text{Jy}$.

Source Name	FWHM (arcmin)	90- μm (Jy) Best est.	170- μm FWHM flux densities (Jy) Best est.	170- μm FWHM flux densities (Jy) (B1) (B2)		200- μm FWHM flux densities (Jy) Best est. (B1) (B2)		
L1498	7×6	≤ 6.0	68.4±1	132±1	3.04±0.08	100±0.8	124±0.7	7.06±0.1
L1517C	7×5	–	16.6±0.7	21.9±0.2	10.1±0.6	34.9±4	42.6±0.2	15.2±0.6
L1517A	7×5	≤ 3.6	36.8±0.9	42.9±0.5	19.1±0.6	55.9±4	74.1±0.5	25.2±0.6
L1517B	4×3	≤ 0.5	13.3±0.6	14.1±0.4	5.83±0.4	17.9±3	27.8±0.4	9.45±0.4
L1512	7×5	≤ 2.2	77.7±0.5	145±1	3.23±0.6	93.6±0.8	192±0.6	4.60±0.7
L1544	8×4	≤ 4.6	60.3±0.4	131±0.6	17.2±0.1	72.4±0.6	202±1	19.9±0.3
L1582A	7.5×4	$\leq 11^*$	262±3	756±6	164±2	290±3	880±7	261±2
L183	7×5	≤ 1.3	52.9±0.3	191±2	25.7±0.9	63.2±0.7	231±2	46.6±1
L1696A	5×5	≤ 8.9	381±2	428±3	12.9±0.8	516±2	606±6	11.1±0.6
L1709A	8×5	≤ 17	47.1±6	68.0±4	12.8±0.4	77.2±2	138±2	31.9±1
L1689A	4×4	70.8±2	564±7	849±6	470±4	591±6	852±5	473±6
L1709C	8×4	$\leq 9.5^*$	65.5±1	225±1	3.32±0.2	66.0±2	306±1	1.59±0.4
L1689B	7×4	≤ 7.4	108±2	194±1	47.8±1	107±2	226±2	43.2±0.7
L204B	10×5	≤ 9.0	56.7±1	151±2	34.8±1	140±2	272±3	126±4
L63	6×6	≤ 5.7	79.4±1	115±1	60.0±0.4	118±0.8	156±1	105±1.0
B68	4×4	$\leq 4.5^*$	25.8±0.3	65.8±0.3	16.8±0.3	34.8±0.6	85.3±0.3	29.2±0.5
B133	8×3	$\leq 15^*$	72.1±0.9	121±0.4	25.6±0.3	108±1	185±2	41.5±1
L1155C	4×3	≤ 0.7	15.0±0.2	107±0.4	4.66±0.2	13.2±2	143±0.4	4.60±0.4

We followed the standard pipeline data reduction procedure, starting with the edited raw data (ERD) files. The responsivity was calculated using the actual fine calibration source (FCS) responsivity calibration by averaging between adjacent FCS measurements and interpolating. Destructive readouts were discarded in calibrating the data from each individual integration ramp. Saturated readouts and glitches were discarded likewise. Ramps were fitted using a first-order polynomial. Dark currents were subtracted. Drift handling was enabled and chopper vignetting was accounted for. Detector non-linearities were also taken into account. For full details of the data reduction procedure, see Laureijs et al. (2001).

Subsequent upgrades to the calibration routines have not significantly altered the flux estimates of extended sources such as ours. This was checked by re-reducing one source at random using the final version 10 (V10) of the data reduction pipeline. This is the version with which the final ISO data archive will be calibrated in its entirety. The empirical point spread function had been updated between V7 and V10, but this only affected the calibration of point sources for the C-200 camera, so did not affect our data. The only other significant change was the non-linearity response function for very bright sources, which also did not affect our data.

The final absolute calibration errors were estimated to be ± 30 per cent. This is similar to that found by others working with ISOPHOT (e.g. Klaas et al 1997; Lehtinen

et al. 1998). We cross-checked our calibration accuracy by comparison with the Cosmic Background Explorer satellite (COBE) and this confirmed our error estimate (see below).

3 RESULTS

3.1 Images and flux densities

Figures 1–8 present images of our sample of pre-stellar cores at each of the three wavelengths of 90, 170 and 200 μm . The grey-scale range from white (faint) to black (bright) for any given source is set to be the same at all three wavelengths using the full range of the 200- μm data (see Tables 1 & 2). In this way the absolute brightness variation from one wavelength to another can be seen clearly. However, the contour levels are based on the dynamic range at each wavelength so that the structure can be discerned in the fainter images.

It can be seen that the cores show a variety of shapes and appearances. However, the first observation which strikes one when studying these images is that the cores are very much less clearly defined at 90 μm than at the other two wavelengths. In fact, most of the cores are not significantly detected at 90 μm , despite appearing strongly in the images at the other two wavebands. L1689A is detected at 90 μm . We have classified L1582A, L1709C, B68 and B133 as marginal detections at 90 μm , because they either have signal-to-noise ratios of $\leq 5\sigma$, or the peak at 90 μm does not coincide in position with the peak at the longer wavelengths.

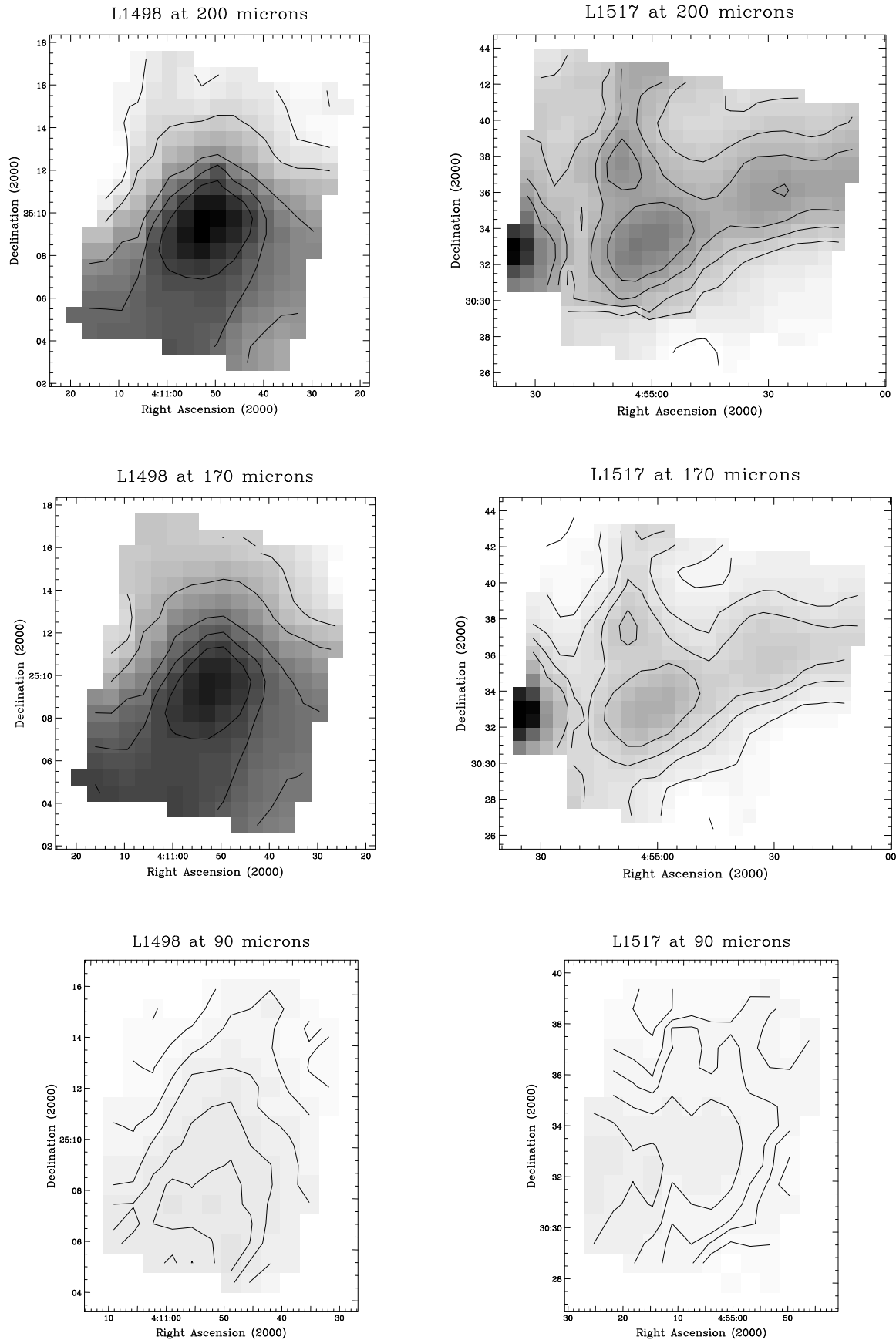


Figure 1. Grey-scale flux density images, with isophotal contour maps superposed, of L1498 (left) and L1517 (right), at 200 (top), 170 (middle) and 90 μm (bottom). In these images, and in Figures 2–8, the grey-scale range from faint (white) to bright (black) for each source is set to be the same at all wavelengths using the full range of the 200- μm data (see Tables 1 & 2). The contour levels are 10, 30, 50, 70 & 90% of the dynamic range at each wavelength.

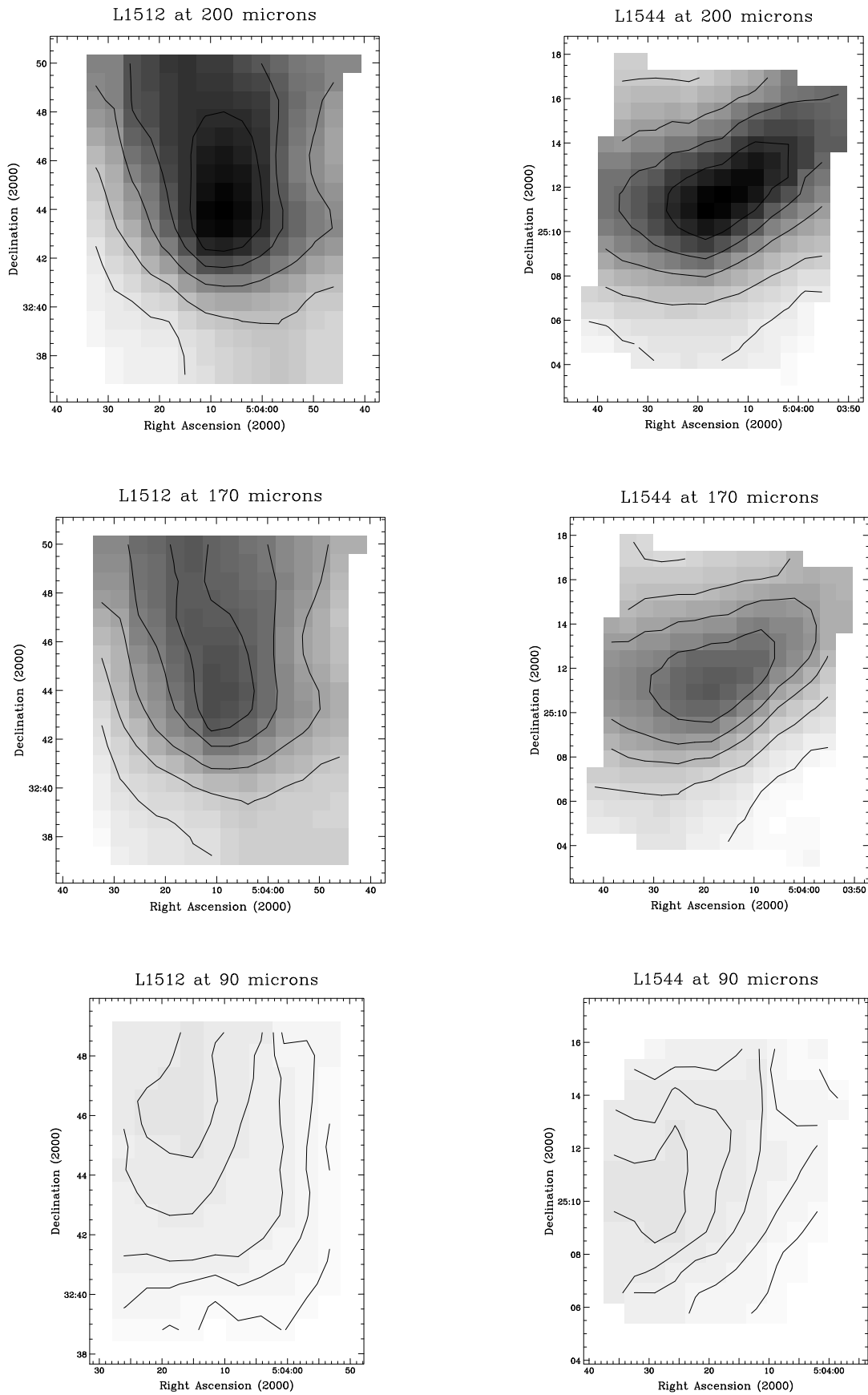


Figure 2. Images of L1512 (left) and L1544 (right). Details as in Figure 1.

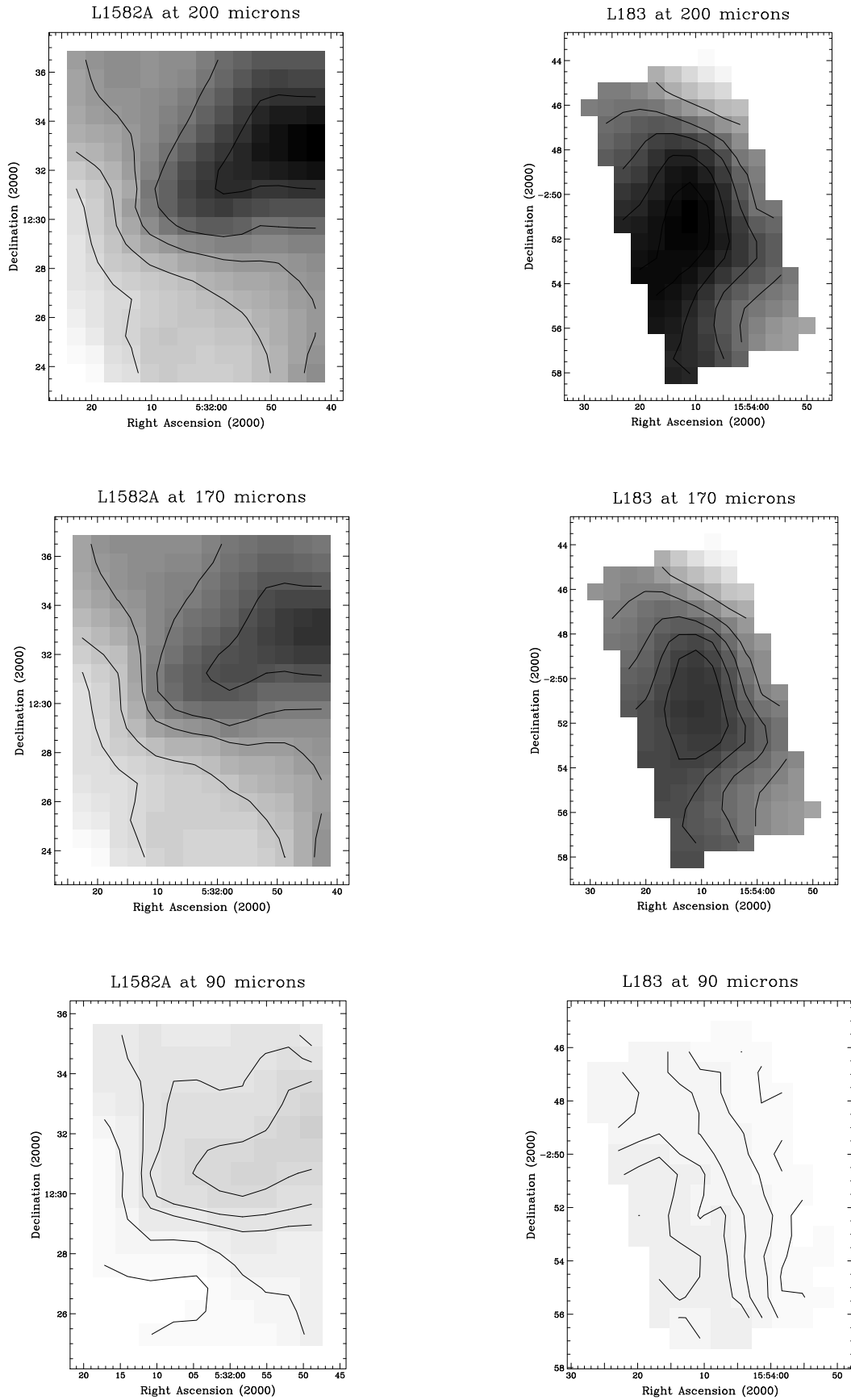


Figure 3. Images of L1582A (left) and L183 (right). Details as in Figure 1.

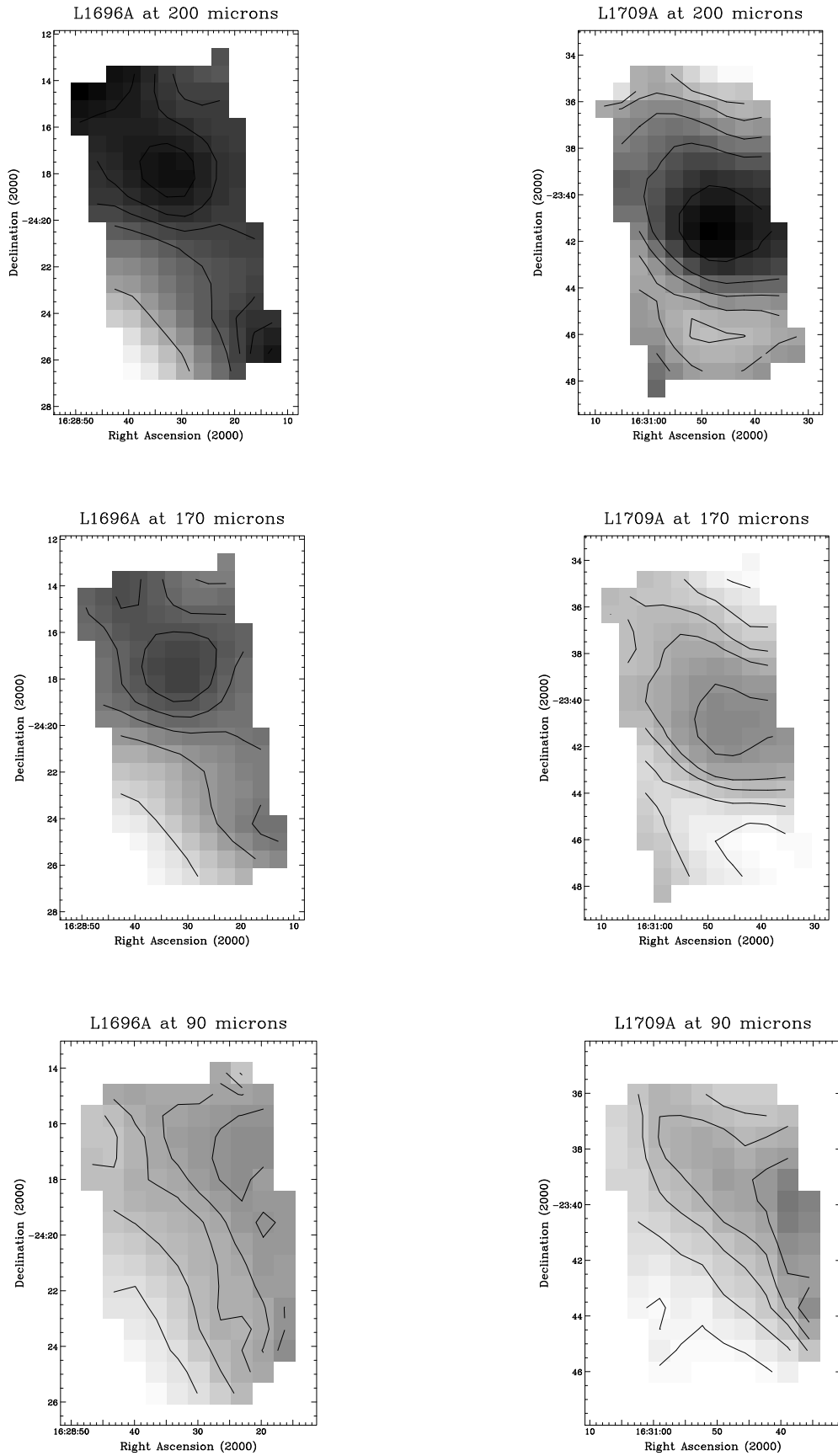


Figure 4. Images of L1696A (left) and L1709A (right). Details as in Figure 1.

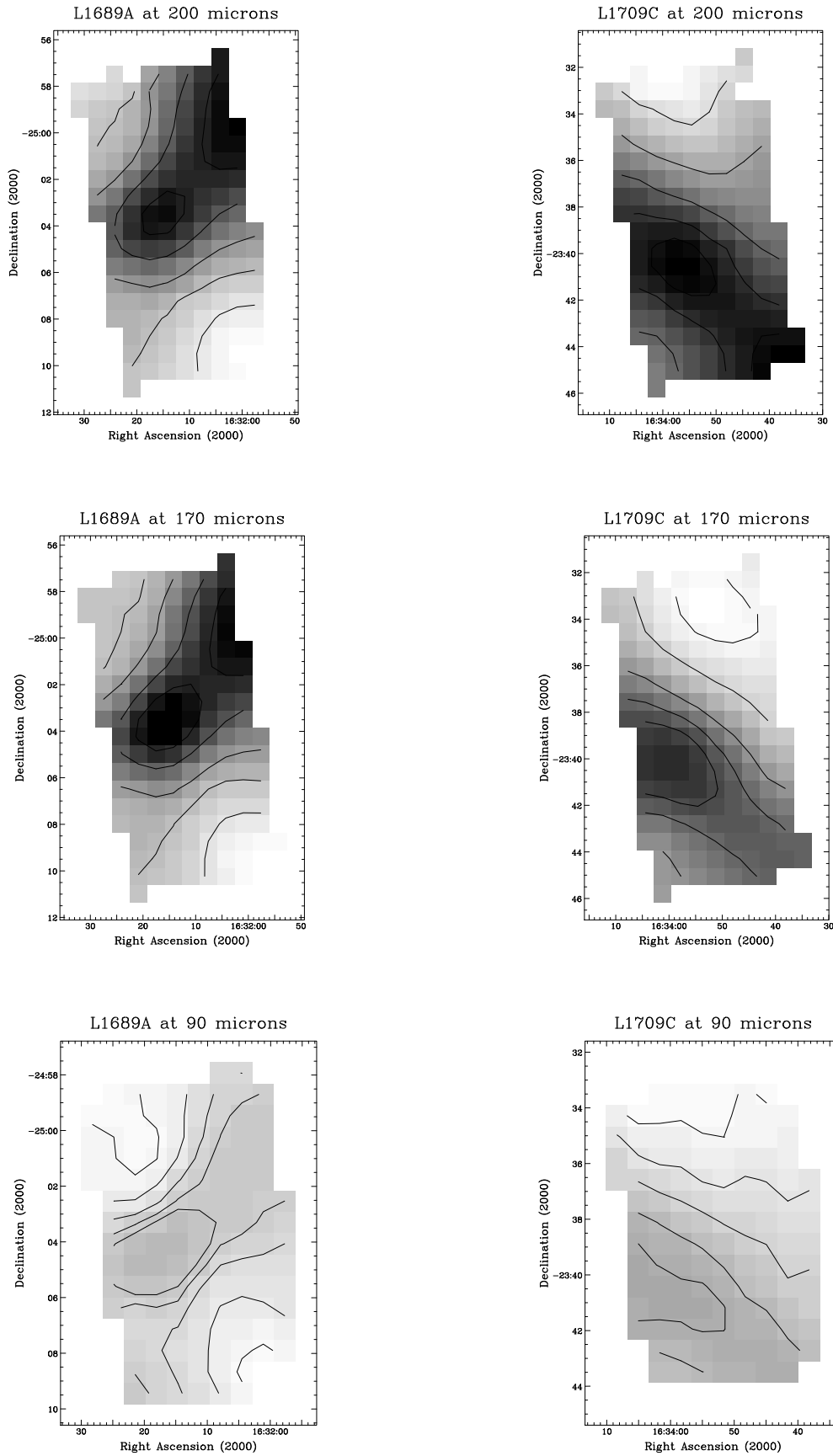


Figure 5. Images of L1689A (left) and L1709C (right). Details as in Figure 1.

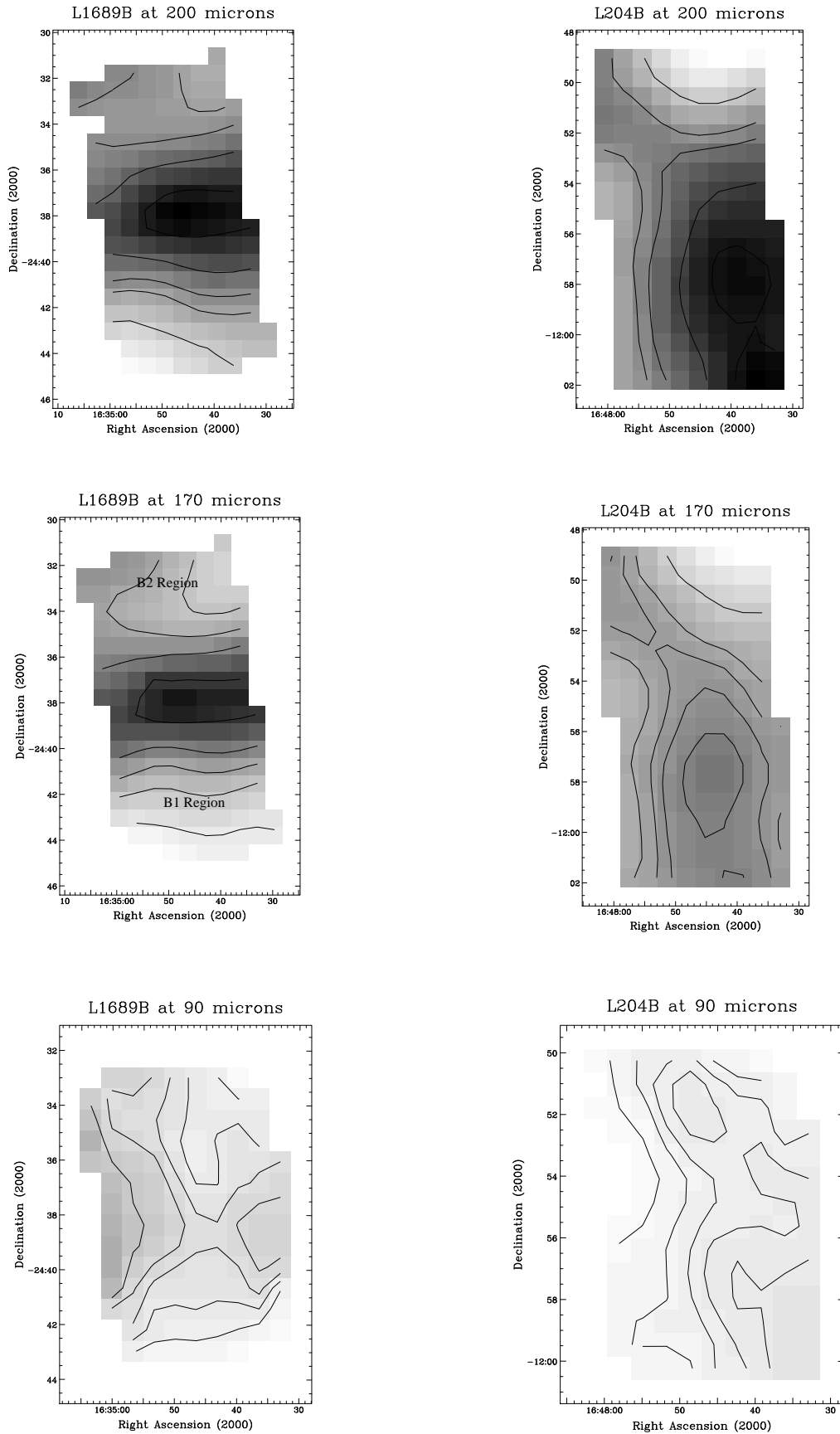


Figure 6. Images of L1689B (left) and L204B (right). Details as in Figure 1.

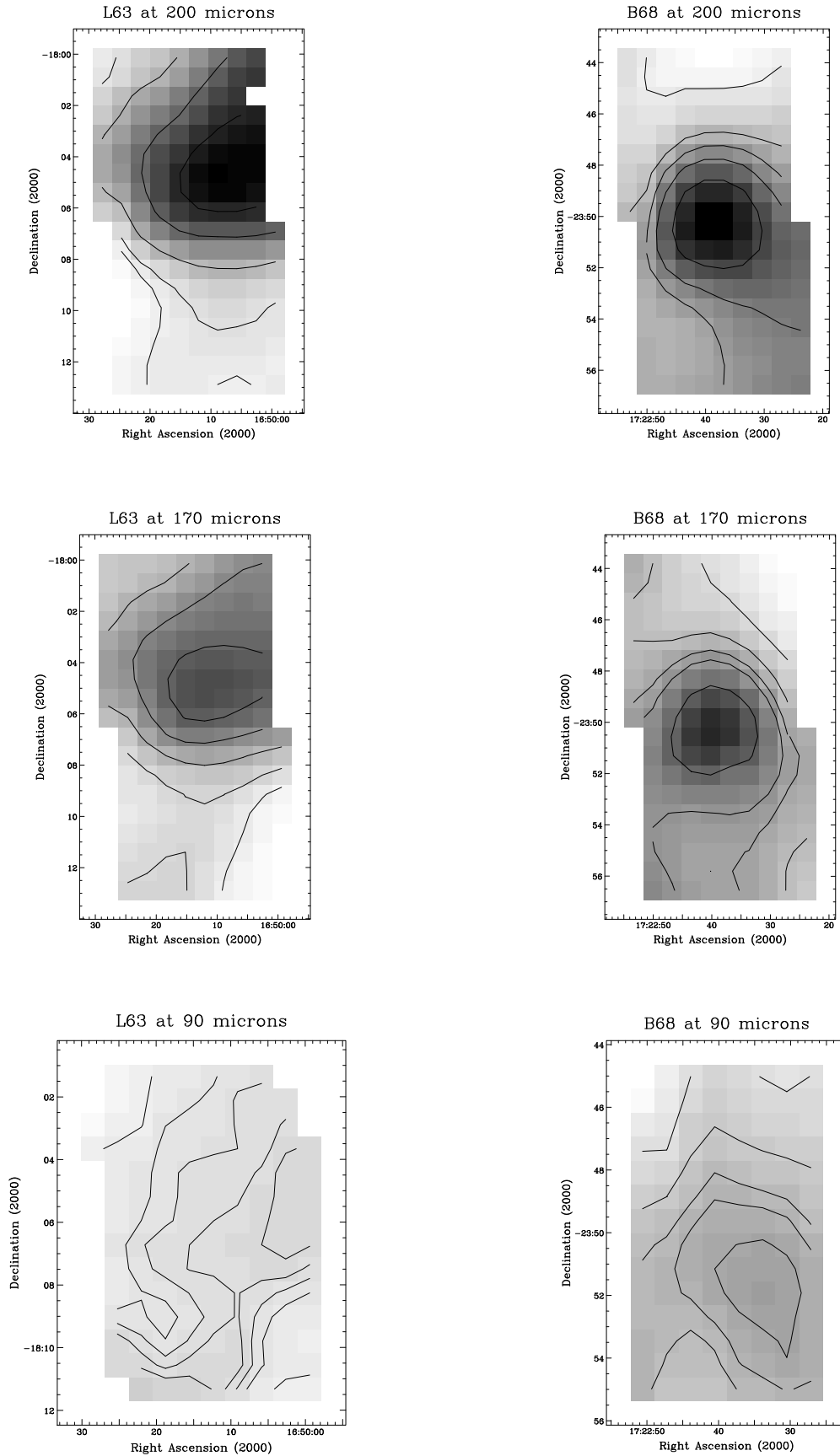


Figure 7. Images of L63 (left) and B68 (right). Details as in Figure 1.

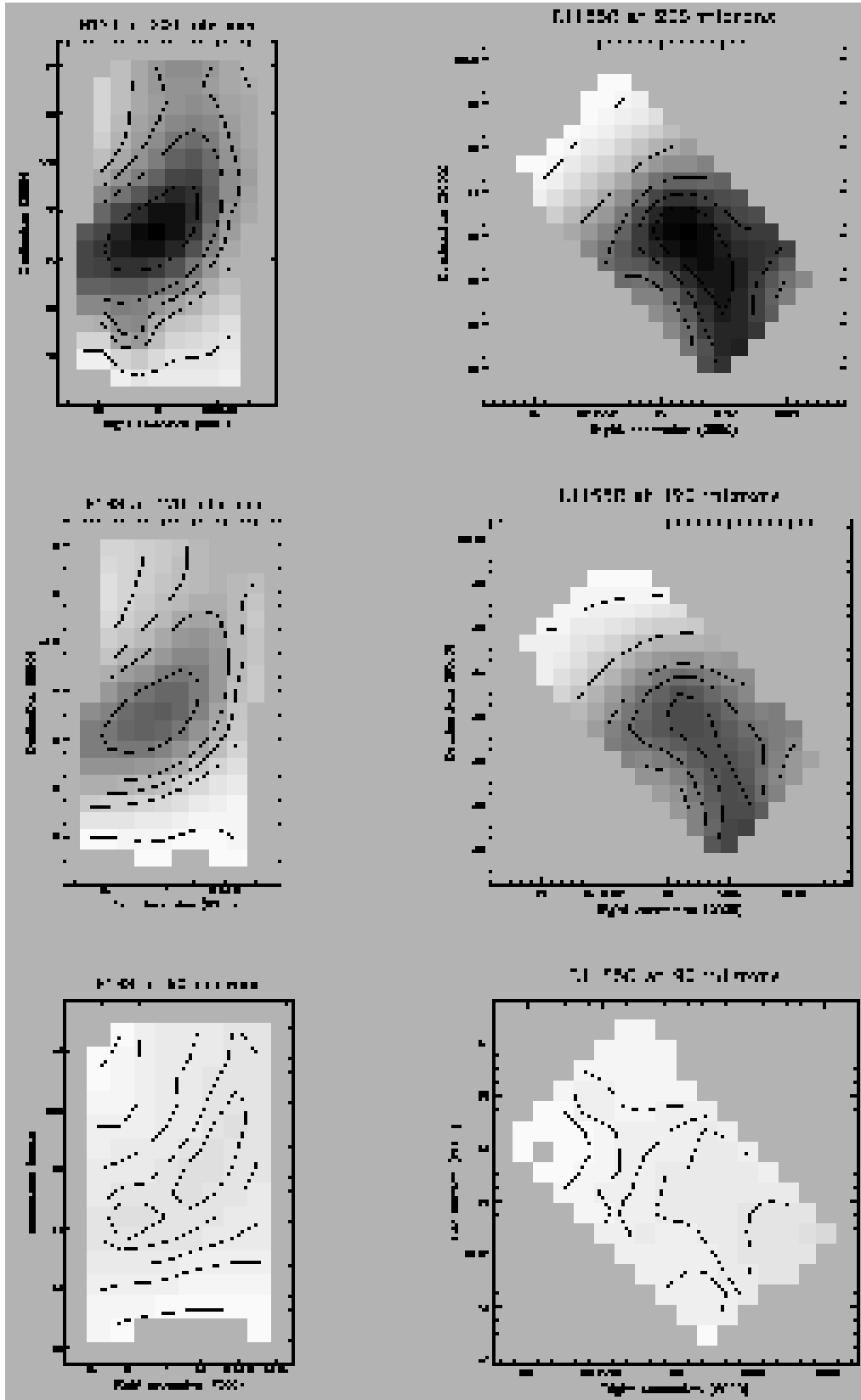


Figure 8. Images of B133 (left) and L1155C (right). Details as in Figure 1.

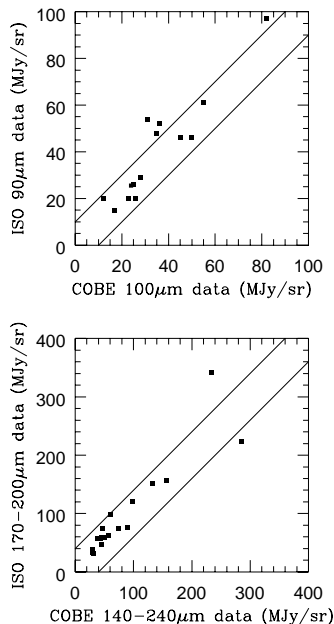


Figure 9. Comparison of ISO calibration with COBE data. The upper panel shows our estimated 90- μm background plotted against the DIRBE 100- μm background for each mapped region. The lower panel shows the mean of our 170- and 200- μm backgrounds plotted against the mean of the DIRBE 140- and 240- μm backgrounds in each region.

Consequently, in each of these cases, it is not clear that the actual core itself has been detected. We may either be detecting the extended cloud, or a different, warmer source in the same cloud. As a result, we do not include any of these sources in our subsequent analysis.

Table 1 lists some of the principle measurements of our target sources. Column 1 lists the source name, wherein we follow the naming convention of Benson & Myers (1989). Columns 2 & 3 list the source positions as measured from the images in Figures 1–8. If there was a discrepancy in source peak position from one wavelength to another, then the 200- μm peak position was taken. The final six columns list the peak flux density of each source at each wavelength (in MJy/sr) and the total integrated flux density measured in the whole of each mapped area. In the case of the 90- μm data the brightest point does not coincide with the core in most sources, so each one is listed as an upper limit. The exception is L1689A, which was the only core to be clearly detected at 90 μm .

The cores exhibit a variety of structures, and in some cases extend beyond the boundaries of the mapped areas. This is because before ISO no-one had imaged these objects at any infra-red wavelength – none were detected by IRAS. Consequently, in setting up these observations we had little guidance as to how big to make the maps, and exactly where to position them. We used as our guide the previous CO and ammonia maps (Benson & Myers 1989 and references therein). Nonetheless, in most cases we have successfully imaged the cores and extended the maps far enough to estimate the background level at each waveband in each field, as we now describe.

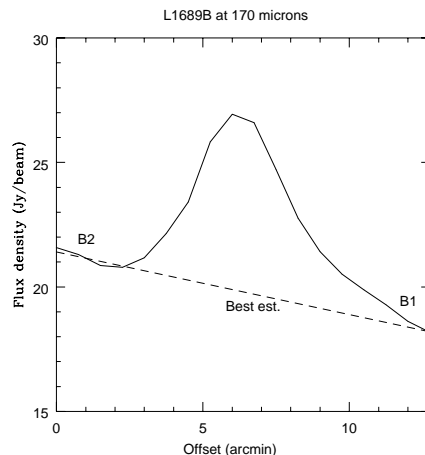


Figure 10. North-south flux density profile through L1689B at 170 μm , at R.A. (2000) of $16^{\text{h}} 34^{\text{m}} 48.8^{\text{s}}$, and from Dec. (2000) of $-24^{\circ} 31' 50''$ to $-24^{\circ} 44' 40''$. Notice how the core sits on a sloping background from the B2 level in the north to the B1 level in the south. The 1σ standard deviation in the B1 and B2 regions after removing this sloping background is 0.56Jy/beam.

3.2 Background subtraction

The infrared background arises from a number of causes, including Zodiacal emission, and large-scale Galactic plane emission. IRAS detected these extended background emissions (Beichman et al 1988; Jessop & Ward-Thompson 2000), as did the Diffuse Infrared Background Experiment (DIRBE) on the COBE satellite. IRAS did not cover wavelengths beyond 100 μm , but DIRBE extended out to 240 μm . Consequently, we chose to compare our background measurements with DIRBE. We estimated the background from the lowest emission region of each map (the same region at each wavelength) and called this background estimate B1. The values of the backgrounds that we measured are listed in Table 2. A comparison between our B1 background estimates and the COBE data is plotted in Figure 9.

Figure 9(a) shows the background (B1) determined from our ISO 90- μm data plotted against the DIRBE measurement at 100 μm which was closest on the sky to our source. Figure 9(b) plots the mean of our 170- and 200- μm background measurements against the mean of the DIRBE 140- and 240- μm background determinations at the closest position on the sky.

In each case we are not comparing exactly like with like. The exact wavelength and filter bandwidths do not match. Likewise the resolutions of the two telescopes do not match – DIRBE had much lower resolution. In addition our background measurements may be slight over-estimates due to the finite size of our images.

Consequently we would not expect an exact correlation between the two data-sets, and we would expect a certain degree of scatter. Nonetheless, the broad agreement at all wavelengths is very encouraging. The spread indicated by the two solid lines on each plot corresponds to roughly ± 30 per cent for mean background levels. This tends to support our assertion above that the absolute calibration uncertainty is no worse than ± 30 per cent.

Table 3 lists the extended source flux densities at each wavelength. In an attempt to separate the compact emission

due to the pre-stellar cores from the extended background emission at 170 & 200 μm , we subtracted the background level (B1) from every field as estimated from the lowest emission region in each image. We then measured the FWHM extent of each source at 200 μm along the maximum and minimum directions. These were occasionally tricky to estimate if the source extended beyond the edge of the mapped region, and some judgement was required in these cases. We measured the flux density at each wavelength for each object within this FWHM in the resulting images. These flux densities are listed in Table 3 under the columns headed B1.

We note that in every case the pre-stellar cores also appear to sit on top of more extended emission that is probably related to the larger scale cloud in which the core is embedded. This can be seen if we take a 1-D north-south cut through the core L1689B at 170 μm . This is shown in Figure 10. It can be seen from this plot that the background in the north is considerably higher than that in the south. We estimated this higher ‘background’ region due to extended cloud emission and called this background B2. The two regions B1 & B2 are shown in Figure 6(a) to illustrate this process.

We attempted to estimate the value of the B2 background emission by measuring the mean flux density in the region of each image where there was extended emission, but away from the core itself. The measured values of the B2 backgrounds are listed in Table 2. We then subtracted these values from each image and re-measured the flux density within the FWHM. These flux densities are listed in Table 3 under the columns headed B2.

Finally, we made our best estimate of the background level in each region, by fitting a sloping background to each region and subtracting this from the core emission. The example of this sloping background in the case of L1689B is illustrated in Figure 10. We measured the FWHM of each source on the resulting images, and list these FWHM in Table 3. We measured the flux densities within these FWHM for each core and list these in Table 3 under the columns headed ‘Best est’.

Thus Table 3 lists the full variation in flux densities at 170 & 200 μm that could be associated with our cores, given the limited sizes of the mapped areas in each case. The errors we list with each measurement are the statistical errors associated with each individual background subtraction. At 90 μm we did not detect most of the 200- μm sources, so we simply list our best estimate of the upper limit to the flux density in each region, based on the 3σ variation in the local background.

3.3 Colour temperatures

We measured the colour temperature variation across each core by first subtracting the background level that we had measured in each image according to our best estimate, as described above. We then ratio-ed the background-subtracted images at 170 and 200 μm . We converted this to a colour temperature using the assumption of optically thin grey-body emission (see section 3.4 below), namely:

$$(F_{\nu_1}/F_{\nu_2}) = \frac{\nu_1^{3+\beta}(e^{[h\nu_2/kT]} - 1)}{\nu_2^{3+\beta}(e^{[h\nu_1/kT]} - 1)},$$

where the frequencies ν_1 and ν_2 correspond to wavelengths of 200 and 170 μm respectively, and F_{ν_1} and F_{ν_2} are the flux densities at each of these frequencies. T is the dust temperature, β is the dust emissivity index, and h and k are the Planck and Boltzmann constants respectively. This is one of the simplest sets of assumptions that can be made, as it assumes that all of the dust in a given pixel is at a single temperature, T , and that it is exactly the same dust which is emitting at both wavelengths. We used $\beta=2$ to fit the data, as we found this to be the typical value for these cores (see section 3.4 below). Using these assumptions we constructed a series of colour temperature maps.

Examination of these maps showed us that for 8 of the 18 cores in our target sample there is no structure in the colour temperature maps that could be associated with the cores. Either there is just a uniform temperature across the field, or else a uniform temperature gradient that is clearly associated with the larger scale cloud, rather than the core itself. These 8 sources are: L1517C, L183, L1696A, L1709C, L63, B68, B133 & L1155C. The colour temperature map of L1689B appears to have a saddle-like geometry, with an increasing gradient from the centre in one direction, and a decreasing gradient orthogonal to this. We believe this may arise due to not having mapped the whole core or a lack of signal-to-noise off source. In the regions of high signal-to-noise ratio, it is slightly cooler at the centre than the edge.

All of the remaining 9 cores show a temperature gradient approximately centred on the core. 8 sources show a gradient which is cooler at the centre than the edge. These are L1498, L1517A&B, L1512, L1544, L1582A, L1709A & L204B. Only one core appears warmer at the centre than the edge, L1689A. We note that cores which are cooler at their centres than their edges are qualitatively consistent with external heating by the local inter-stellar radiation field (ISRF).

Figure 11 shows colour temperature maps of six cores as grey-scale images with contours from the 170- μm background-subtracted (‘Best est.’) flux density images superposed. The values of the colour temperatures were not calculated above 50K, as the 170- to 200- μm flux density ratio is not sensitive to temperatures in this range. Typically values of this sort were only found at the edges of the images, where the signal-to-noise ratio was low, and hence such values were cut out of the images in Figure 11.

We show one example of a uniform temperature core, B68, although we note that even this source has tentative evidence for being warmer at its edge. We show one example of a large-scale temperature gradient, L1696A. We note that this source has a temperature peak to the northwest of the core. This may be due to asymmetric heating by nearby young stars causing one side of the core to be warmer than the other. We illustrate 3 cores that are cooler at the centre than the edge, L1498, L1512 & L1544 (we note that in the case of L1498 we only see the temperature gradient on one side of the core due to only having partial maps of the region). We also show the core that appears warmer at the centre than the edge, L1689A. Thus these six sources illustrate the variation in the colour temperature maps that we see.

The fact that none of the cores except L1689A shows a strong central temperature peak indicates that none (except possibly L1689A) has a central protostar yet, as was

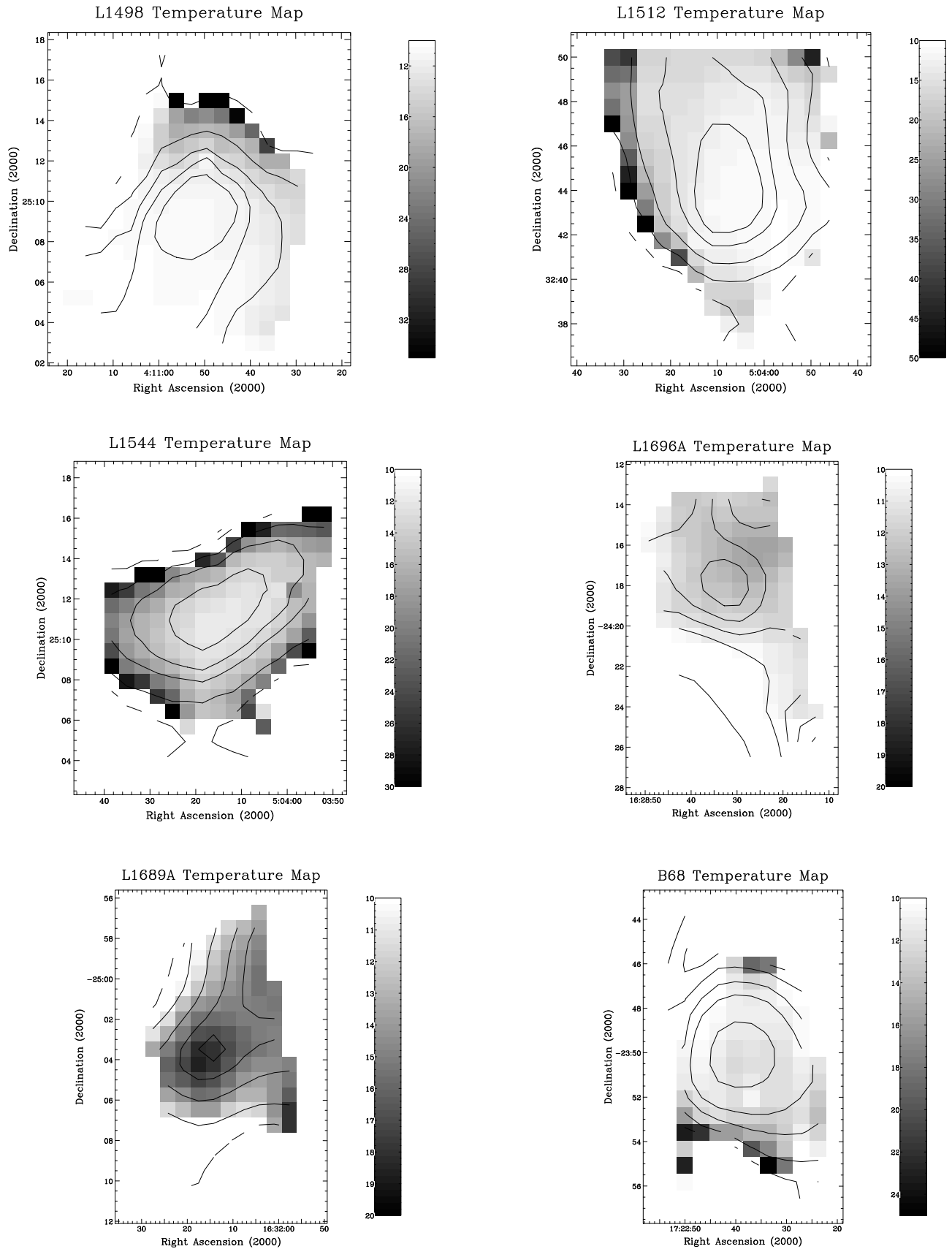


Figure 11. ISOPHOT 170/200- μm colour temperature grey-scale images of L1498, L1512, L1544, L1696A, L1689A & B68, superposed on contours of 170- μm flux density. The grey-scale bars in each figure show the values of the colour temperatures in K.

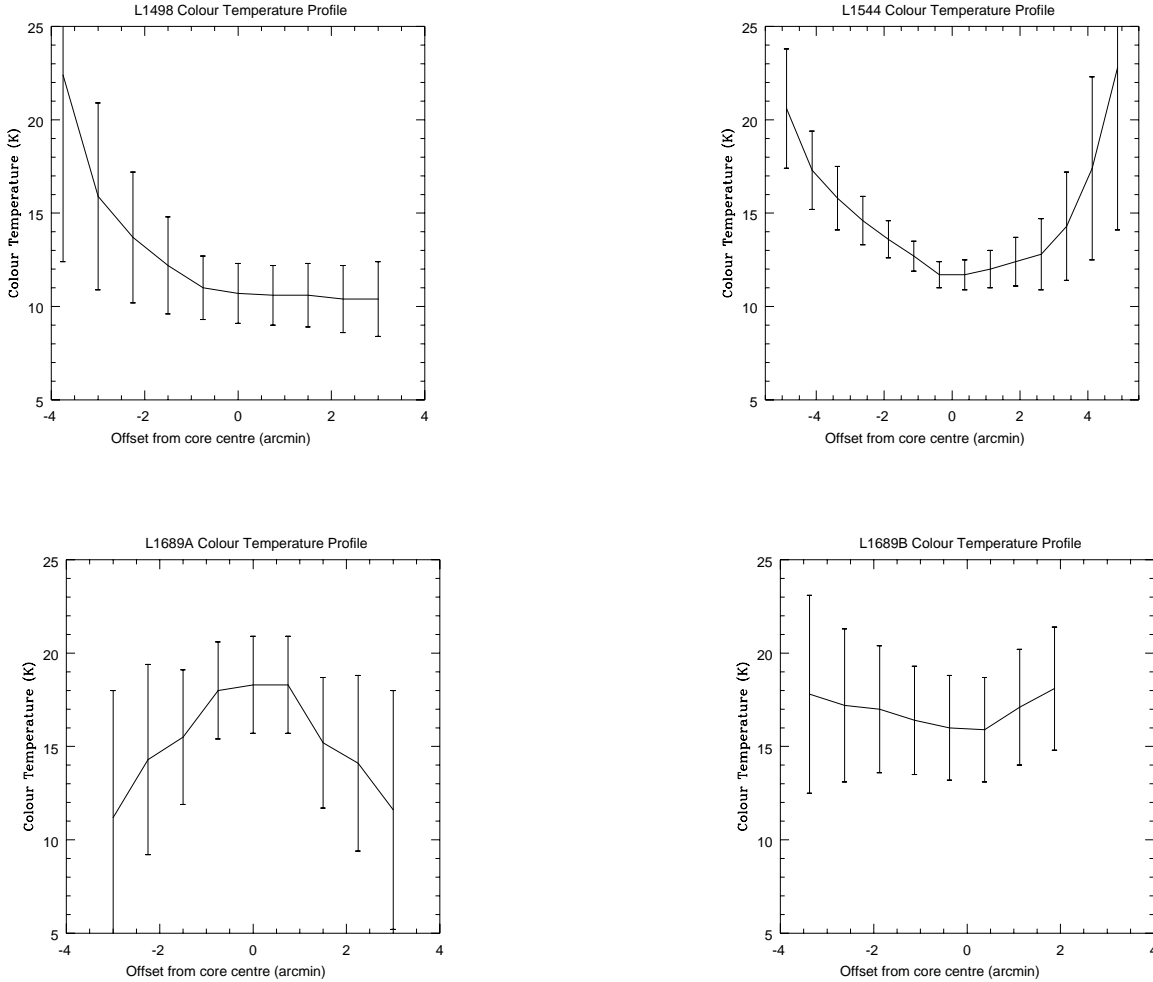


Figure 12. 1-D colour temperature profiles through L1498 (NW→SE), L1544 (E→W), L1689A (SW→NE) and L1689B (E→W).

suspected, and hence they are confirmed as pre-stellar in nature. The cores which are clearly cooler at their centres than their edges show the behaviour one would qualitatively expect for externally heated cores. The remainder are consistent with being in isothermal equilibrium. We also note that the only core with a strong temperature gradient where the centre is warmer than the edge, L1689A, is also the only core with a clear $90\text{-}\mu\text{m}$ detection. Therefore L1689A is clearly different from the rest of our sample. It may be more evolved than the other cores and contain an embedded protostar. We think this is unlikely since its submillimetre flux densities are lower than some of the other cores, such as L1689B (Paper I). Alternatively, it may simply be warmer due being more diffuse, and hence more prone to heating throughout the core by the surrounding environment.

Figure 12 shows cuts through the colour temperature maps, with error-bars, of three cores that appear cooler at their centres, L1498, L1544 and L1689B, and the core that is warmer at the centre, L1689A. The difference in appearance between the colour temperature profiles of L1544 and L1689A is most marked. The temperature gradients we observe are larger than our calculated error-bars for all except

L1689B, which shows the least temperature variation of the four. In all cases there appears to be a central region of roughly uniform temperature. In the case of L1498 the core appears to lie at the end of a ridge extending to the south-east, and the temperature appears uniform along this ridge, rising at the northwestern side of the core. Of the 9 cores (including L1689B) which appear cooler at their centres, 4 have gradients larger than the error-bars, L1498, L1544, L1512 and L1582A. The core that is warmer at its centre, L1689A, also has a gradient larger than the error-bars. All of the remaining cores are consistent with being isothermal to within a 1σ error of typically 2–4 K.

3.4 Spectral energy distributions and luminosities

We can combine the ISOPHOT data presented in this paper with data taken at other wavelengths to calculate the spectral energy distribution (SED) of some of these pre-stellar cores. We also have millimetre and submillimetre data (Papers I–III, Kirk et al. in prep.) of some of the cores. These data only cover the central region of each core, in which even those cores with temperature gradients at their edges appear

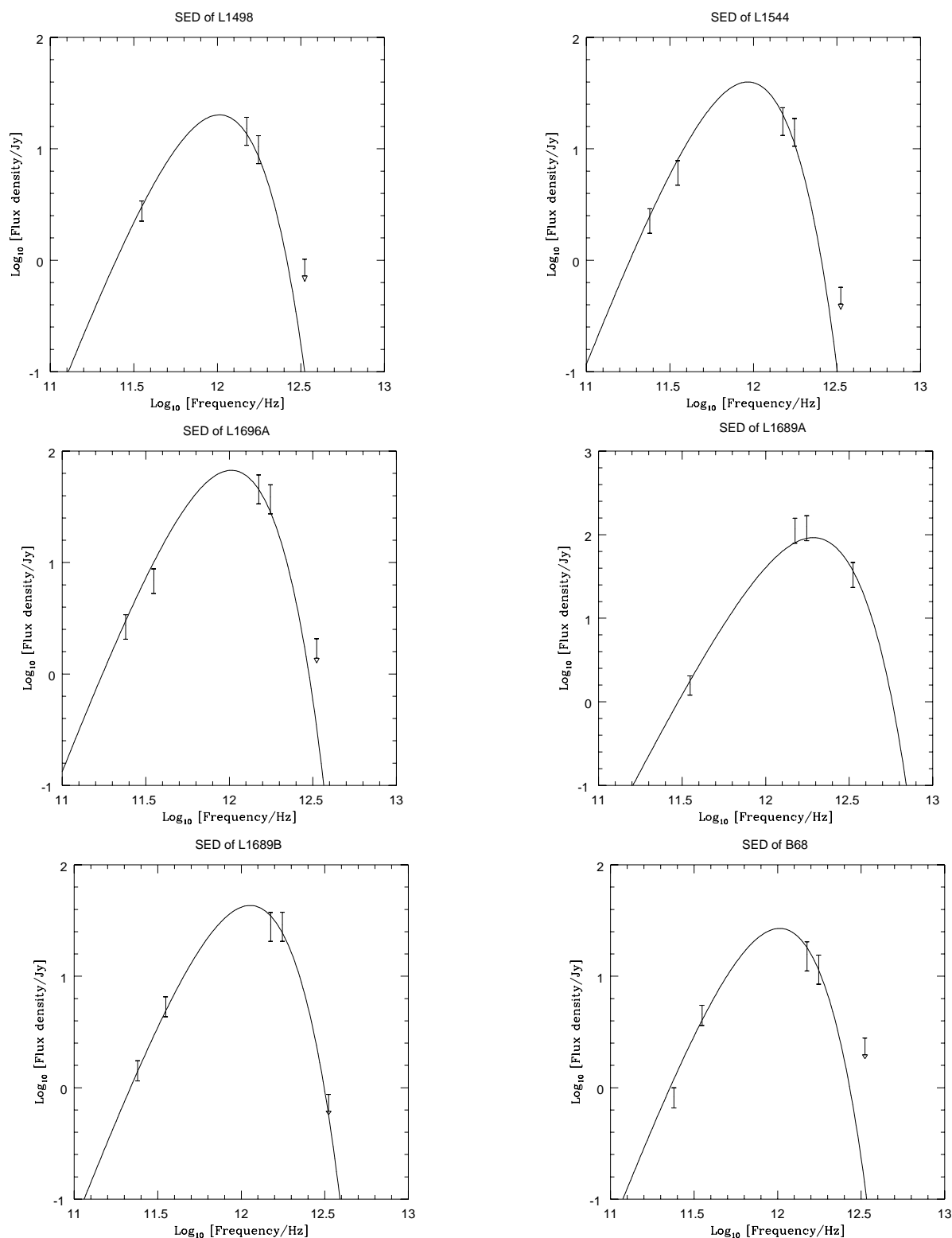


Figure 13. Spectral energy distributions of the cores L1498, L1544, L1696A, L1689A&B and B68. See text for discussion.

isothermal. Thus we used the isothermal approximation in modelling the SEDs of the cores, and concentrated on those cores which have been best studied.

We measured the flux density on the best estimate background-subtracted images in a circular aperture of diameter 150 arcsec at each wavelength for each of our sources,

to match the largest aperture for which we have mm/submm flux densities available, and list the measured flux densities in Table 4. We compared these with the flux densities measured at millimetre (Papers II & III) and submillimetre wavelengths (Paper I; Kirk et al. in prep.) measured in the same size apertures. We plot these data on a logarithm-

Table 4. Extended source flux densities measured in a 150-arcsec diameter aperture centred on the 200- μm peak position, as measured from the ‘Best est.’ background-subtracted maps. These are used in combination with mm/submm data to generate spectral energy distributions. The upper limits and error-bars are based on background fluctuations. Calibration errors are $\pm 30\%$.

Source	S_{90} (Jy)	S_{170} (Jy)	S_{200} (Jy)
L1498	≤ 1.02	10.4 ± 0.4	15.2 ± 0.3
L1517C	–	5.79 ± 0.4	11.4 ± 2.0
L1517A	≤ 1.23	9.64 ± 0.4	14.1 ± 2.0
L1517B	≤ 0.78	5.90 ± 0.4	8.39 ± 2.0
L1512	≤ 1.40	11.8 ± 0.2	16.2 ± 0.3
L1544	≤ 0.57	14.9 ± 0.2	18.6 ± 0.3
L1582A	≤ 10.6	53.7 ± 1.0	59.8 ± 1.0
L183	≤ 0.28	10.4 ± 0.1	12.4 ± 0.3
L1696A	≤ 2.07	38.7 ± 0.8	47.5 ± 1.0
L1709A	≤ 1.60	10.3 ± 3.0	17.5 ± 0.7
L1689A	34.5 ± 1	125 ± 3.0	117 ± 3.0
L1709C	≤ 5.72	19.9 ± 0.6	19.6 ± 0.8
L1689B	≤ 0.87	29.1 ± 0.8	29.0 ± 0.9
L204B	≤ 1.05	11.1 ± 0.5	24.9 ± 0.9
L63	≤ 2.69	19.2 ± 0.5	28.5 ± 0.4
B68	≤ 2.79	12.0 ± 0.2	15.8 ± 0.4
B133	≤ 4.46	22.6 ± 0.5	34.6 ± 0.7
L1155C	≤ 0.69	8.12 ± 0.1	7.42 ± 1.0

mic scale, as a function of frequency, in Figure 13, for the sources L1498, L1544, L1696A, L1689A&B and B68.

Also plotted on Figure 13, are a series of modified black-body, or grey-body, curves of the form:

$$F_\nu = B_{\nu,T}(1 - e^{-\tau_\nu})\Omega$$

where F_ν and $B_{\nu,T}$ are the flux density and black-body emission respectively, at frequency ν . T is the dust temperature, Ω is the solid angle of the source and τ_ν is the optical depth at frequency ν , which is usually given in the form $\tau_\nu \propto \nu^\beta$. The solid curves shown in Figure 13 all have $\beta=2$ and $\tau_{200\mu\text{m}}=0.06$, and have dust temperatures of $T=10\text{K}$ for L1498, $T=9\text{K}$ for L1544, $T=10\text{K}$ for L1696A, $T=19\text{K}$ for L1689A, $T=11\text{K}$ for L1689B, and $T=10\text{K}$ for B68. We note that $\tau_{200\mu\text{m}}=0.06$, making typical assumptions about dust mass opacity (e.g. Hildebrand 1983), corresponds to a central column density of $N_{\text{H}_2}^{\text{Central}}=7 \times 10^{22} \text{cm}^{-2}$. This is consistent with the values we estimate in these cores (see Table 5).

We estimate that the error-bars on the temperatures are typically $\pm 3\text{K}$. These were calculated by measuring the flux densities in a 150-arcsec aperture for each source at each wavelength on the images derived from the B1 and B2 background subtractions, since this represents the dominant source of error. Then grey-body curves were fitted through these flux densities and their temperatures were derived. In this way the maximum possible shift in temperature was calculated, and found to be around $\pm 3\text{K}$. We note that the hottest core, L1689A, is the only core where we see a temperature gradient that decreases towards the edge. It is therefore obvious that L1689A is different from the other cores in more than one way, and its status is unclear.

The total far-infrared and mm/submm luminosity radiated by each core, $L_{\text{out}}^{\text{SED}}$, can be calculated by integrating

under the solid curves of Figure 13. We list these luminosities in Table 5. We also list the central column density (e.g. Paper III; Bacmann et al. 2000) and assumed distance of each of the cores, as well as the direction of the temperature gradient derived above, and details of whether the core was seen in absorption by ISOCAM (Bacmann et al. 2000). The incident luminosity on each core is listed in column 5 of Table 5, and we now address the manner in which this was calculated.

4 ENERGY BUDGET OF THE CORES

If the cores in our sample are truly starless, the total luminosity emitted by each core is not expected to exceed the amount of radiation incident upon the core. The present ISO results allow us to check this quantitatively for the first time in these cores. We can indeed compare the measured output SED luminosities ($L_{\text{out}}^{\text{SED}}$) with estimates of the input luminosities ($L_{\text{in}}^{\text{ISRF}}$) provided by the local inter-stellar radiation field (ISRF). The local ISRF directly incident on each core is not precisely known but can be roughly estimated from the mid-IR and far-IR backgrounds observed towards each core by ISOCAM (Bacmann et al. 2000) and ISOPHOT (this paper).

The radiation field within a molecular cloud is believed to consist of two main components (Mathis, Mezger, & Panagia 1983): one component that we shall refer to as the ‘near-IR’ component, since it peaks at $\sim 1\text{--}5\ \mu\text{m}$, (but note that this also includes the optical and UV radiation); and another component that we shall refer to as the ‘far-IR’ component, since it peaks at $\sim 100\text{--}200\ \mu\text{m}$.

For simplicity, we assume that the spectral shapes of these components are the same as for the average ISRF in the solar vicinity (see figure 1 of Mathis et al. 1983). However, we can allow for the fact that the strengths of the two ISRF components vary from core to core and sometimes differ substantially from the strengths estimated by Mathis et al. for the average solar ISRF (outside molecular clouds), which are: $I_{\text{ISRF}}^{\text{Mathis}}(7\ \mu\text{m}) \sim 0.1\ \text{MJy/sr}$ and $I_{\text{ISRF}}^{\text{Mathis}}(200\ \mu\text{m}) \sim 6\ \text{MJy/sr}$.

The mid-IR Zodiacal emission was taken from Bacmann et al. (2000). The 200- μm Zodiacal emission was estimated to be typically only $\sim 1.5\ \text{MJy/sr}$ from a model based on COBE data (c.f. Kelsall et al. 1998), which is much smaller than the values listed in Table 2. In fact we see that the near-to mid-IR and far-IR backgrounds (after subtraction of the Zodiacal foreground emission) measured by ISO towards the cores are indeed significantly larger than the Mathis et al. values in all cases.

This is not surprising since the mid-IR background emission is thought to arise from very small (PAH-like) grains excited by the local far-UV radiation field in the outer ($A_V \lesssim 1$) envelopes of molecular clouds (e.g. Bernard et al. 1993), and the far-IR radiation field deep inside a cloud is known to be much stronger than the Galactic far-IR radiation field (Mathis et al. 1983). Furthermore, in the ρ Oph complex, the external far-UV field is estimated to be a factor of $\sim 10\text{--}100$ times brighter than the average far-UV field in the solar neighbourhood (Liseau et al. 1999).

To obtain a realistic estimate of the local ISRF around each core, we have scaled the strengths of the near-IR and

Table 5. Source properties of some of the best studied cores. The SED temperature comes from fits such as those in Figure 13. The temperature gradient was derived from studies such as those shown in Figures 11 and 12, and is marked ‘in’ if the centre is warmer than the edge, ‘out’ if the centre is cooler, and ‘0’ if there is no gradient. The output luminosity L_{out}^{SED} is measured by integrating under grey-body fits such as those shown in Figure 13. The input luminosity L_{in}^{ISRF} is derived from the estimated local radiation field incident upon the core (see text). The central column density $N_{H_2}^{Central}$ is taken from Paper III, Bacmann et al. (2000) & Kirk et al. (in prep). The column headed ISOCAM absorption indicates whether the cores were seen in absorption by ISOCAM (Bacmann et al. 2000). The typical error-bars on the temperature estimates are ± 3 K (see text for details).

Core Name	SED Temp. (K)	Colour Temp. Gradient	L_{out}^{SED} (L_{\odot}) (150-arcsec)	L_{in}^{ISRF} (L_{\odot}) (150-arcsec)	Assumed Distance (pc)	$N_{H_2}^{Central}$ (cm^{-2})	ISOCAM Absorption
L1498	10	out	0.1	0.06	140	5×10^{22}	–
L1517B	10	out	0.08	0.05	140	4×10^{22}	Y
L1544	9	out	0.2	0.1	140	6×10^{22}	Y
L1582A	15	out	4.0	1.5	400	3×10^{22}	Y
L183	10	0	0.15	0.05	150	7×10^{22}	–
L1696A	10	0	0.3	0.6	140	7×10^{22}	Y
L1689A	19	in	0.8	0.5	140	2×10^{22}	N
L1689B	11	out	0.3	0.5	140	6×10^{22}	Y
L63	11	0	0.2	0.06	160	5×10^{22}	–
B68	10	0	0.3	0.2	200	3×10^{22}	N
B133	13	0	2.3	0.6	400	4×10^{22}	N

far-IR components of the Mathis et al. radiation field according to the observed values of the mid-IR and far-IR backgrounds (c.f. table 2 of Bacmann et al. 2000 and Table 2 of this paper). We also account for the fact that a substantial fraction of the near-IR (plus UV and optical) component is absorbed by the parent molecular cloud before reaching the surface of the core, which is at a typical depth of $A_V^{depth} \sim 2-10$.

We thus assume that the effective radiation field incident on the core is:

$$I_{ISRF}^{eff}(\lambda) = [I_{back}^{ISOCAM}(7 \mu\text{m}) / I_{ISRF}^{Mathis}(7 \mu\text{m})] \times I_{ISRF}^{Mathis}(\lambda) \times \exp(-\tau_{\lambda}^{depth})$$

from $0.09 \mu\text{m}$ to $20 \mu\text{m}$, and:

$$I_{ISRF}^{eff}(\lambda) = [I_{back}^{ISOCAM}(200 \mu\text{m}) / I_{ISRF}^{Mathis}(200 \mu\text{m})] \times I_{ISRF}^{Mathis}(\lambda)$$

between $20 \mu\text{m}$ and $1000 \mu\text{m}$. Adopting a spherical core geometry, we compute the effective ISRF flux density absorbed by the core as:

$$F_{ISRF}^{abs}(\lambda) = 2\pi I_{ISRF}^{eff}(\lambda) \int_0^1 [1 - \exp(-\tau_{core}(\mu, \lambda))] \mu d\mu,$$

where $\mu = \cos\theta$ is the cosine of the angle that a ray makes with the normal to the surface of the core, and $\tau_{core}(\mu, \lambda)$ is the core optical depth along that ray (see Lehtinen et al. 1998). The integral over angles is calculated numerically using the typical radial column density profile measured by Bacmann et al. (2000).

For example, in the case of L1689B, figure 5(e) of Bacmann et al. (2000) indicates a column density $N_{H_2} \sim 2 \times 10^{22} \text{ cm}^{-2}$ (i.e. $A_V \sim 20$) at an angular radius of 75 arcsec from the core centre. Assuming that the core is embedded roughly mid-way through the cloud, this leads to a depth $A_V \sim 10$ from the cloud surface to the core surface at 75 arcsec radius. τ_{λ}^{depth} is then derived from this A_V us-

ing the extinction curve of Mathis et al. (1983 – c.f. their appendix C).

The total input luminosity provided to the core by the effective incident radiation field is then:

$$L_{in}^{ISRF} = 4\pi R_{core}^2 \int_{0.09 \mu\text{m}}^{1000 \mu\text{m}} F_{ISRF}^{abs}(\lambda) d\lambda,$$

where R_{core} is taken to be the radius corresponding to a $150''$ diameter aperture.

The values of L_{in}^{ISRF} estimated in this way are listed in Table 5. However, note that the spectrum of the ISRF within molecular clouds that we have used in the above calculations is not accurately known (Mathis et al. 1983), as stated above, and dust grain absorption properties are extremely uncertain.

Similarly, the radial density distributions of the cores is not well known in all cases. For three cores (L1544, L1696A, L1689B), L_{in}^{ISRF} was estimated using the radial density structure measured by Bacmann et al. (2000). For the remaining cores the exact radial profile was not so clear, and a typical structure matching the measured central column density in Table 5 was assumed. The values of L_{in}^{ISRF} are more uncertain in these cases.

The density profiles are crucially important in determining the exact fraction of the ISRF that is absorbed by the cores. For example, in the case of L1689B in which we believe we know the density profile quite well, we calculate that only $\sim 10\%$ of the incident flux is absorbed. In this case we see excellent agreement between our calculated value of L_{in}^{ISRF} and our measured value of L_{out}^{SED} . For some of the other cores, given all of the uncertainties, we estimate that the luminosity values in Table 5 may be uncertain by at least a factor of $\sim 2-4$.

A detailed submillimetre survey of the cores would help to remove some of the uncertainties associated with the density structure. Nevertheless, it is encouraging to see that L_{in}^{ISRF} is found to be similar to L_{out}^{SED} in most cases.

We therefore conclude that the cores are generally con-

sistent with heating by the local ISRF, and require no additional central protostellar heating sources. Note that this is true even for those pre-stellar cores, such as L1544, which already have evidence for infall motions (Tafalla et al. 1998). This might be expected, according to some models, since the compressional luminosity due to the work done by the gravitational forces is indeed estimated to be negligible ($\sim 10^{-3} L_{\odot}$) as long as the collapse remains roughly isothermal (e.g. Henriksen 1994). However, it is not consistent with models that require a significant protostar to have formed at the centre of collapsing cores such as L1544. Thus the cores are all consistent with being pre-stellar in nature.

5 CONCLUSIONS

We have presented data taken with ISO, using the long wavelength photo-polarimeter ISOPHOT, of a series of starless cores. We have measured their flux densities and colour temperatures at 90–200 μ m. The higher resolution and longer wavelength coverage of ISO compared to IRAS have allowed us to make colour temperature maps of the cores. We have found that most of the cores are either isothermal, or have a temperature gradient that is cooler at the centre than the edge.

We have fitted spectral energy distributions to the cores that allow us to ascribe dust temperatures to the densest regions of the cores. Subsequent work will be able to use these temperatures to calculate other properties of the cores, such as their masses. We have also used the spectral energy distributions to calculate the luminosities of the cores.

We have compared our ISOPHOT images of emission from cool dust in the cores with our previously published ISOCAM images of absorption by the same dust. We found that by comparing the output luminosity of each core with an estimate of its energy input from the local ISRF, we can conclude that the cores are generally consistent with being pre-stellar in nature and externally heated, with no need for a central heating protostellar source.

ACKNOWLEDGMENTS

The authors wish to thank the ISOPHOT team, and in particular Martin Haas, at the Max Planck Institut für Astronomie (MPIA), Heidelberg, for assistance with calibration of the data.

We would also like to thank the UK ISO support team at the CCLRC (formerly RAL) for providing much necessary information and support. In particular we thank Helen Walker for the answers to many questions, and Phil Richards for software assistance, especially with regard to the calibration errors and the colour temperature analysis.

We are also grateful to Charles Ryter for an enlightening discussion on the ISRF and to Aurore Bacmann for estimates of the mid-IR background. We should like to thank the referee for a number of helpful suggestions.

The Infrared Space Observatory is an ESA project with instruments funded by ESA member states, particularly the PI countries, France, Germany, Netherlands and the United Kingdom, and with the participation of ISAS (Japan) and NASA (USA).

ISOPHOT was built by the ISOPHOT Consortium, and the data presented in this paper were reduced using PIA, which is a joint development by the ESA Astrophysics Division and the ISOPHOT Consortium with the collaboration of the Infrared Processing and Analysis Center (IPAC).

Contributing ISOPHOT Consortium institutes are the Dublin IAS, the UK CCLRC (formerly RAL), AI Potsdam, MPI Kernphysik, and MPIA Heidelberg.

REFERENCES

- André P., 1994, in: Montmerle T., Lada C. J., Mirabel I. F., Tran Than Van J., eds, ‘The Cold Universe’, p. 179, Editions Frontières, Gif-sur-Yvette
- André P., 1997, in: Reipurth B., Bertout C., eds, ‘Herbig-Haro flows and the birth of low-mass stars’, IAU Symp. 182, p. 483, Kluwer, Dordrecht
- André P., Montmerle T., 1994, ApJ, 420, 837 – AM94
- André P., Ward-Thompson D., Barsony M., 1993, ApJ, 406, 122 – AWB93
- André P., Ward-Thompson D., Barsony M., 2000, in: Mannings V., Boss A., Russell S. S., eds., ‘Protostars and Planets IV’, p. 59, University of Arizona Press – AWB00
- André P., Ward-Thompson D., Motte F., 1996, A&A, 314, 625 – Paper II
- Arviset C., Prusti T., 1999, ESA Bulletin No. 98, ‘The ISO Data Archive’, ESA, Noordwijk
- Bacmann A., André P., Puget J.-L., Abergel A., Bontemps S., Ward-Thompson D., 2000, A&A, 361, 555
- Basu S., Mouschovias T. Ch., 1995, ApJ, 453, 271
- Beichman C. A., Myers P. C., Emerson J. P., Harris S., Mathieu R., Benson P. J., Jennings R. E., 1986, ApJ, 307 337
- Beichman C. A., Neugebauer G., Habing H. J., Clegg P. E., Chester T. J., eds, 1988, Infrared Astronomical Satellite Catalogs and Atlases Explanatory Supplement, NASA RP-1190, US Government Printing Office, Washington DC
- Benson P. J., Myers P. C., 1989, ApJS, 71, 89
- Bernard J. P., Boulanger F., Puget J. L., 1993, A&A, 277, 609
- Foster P. N., Chevalier R. A., 1993, ApJ, 416, 303
- Gabriel C., Acosta-Pulido J., Heinrichsen I., Morris H., Tai W. M., 1997, in Hunt G., Payne H. E., eds, ASP Conference Series, 125, 108, ‘Astronomical Data Analysis Software and Systems (ADASS) VI’, Astronomical Society of the Pacific, San Francisco
- Henriksen R., 1994, in: Montmerle T., Lada C. J., Mirabel I. F., Tran Than Van J., eds, ‘The Cold Universe’, p. 241, Editions Frontières, Gif-sur-Yvette
- Henriksen R., André P., Bontemps S., 1997, A&A, 323, 549
- Hildebrand R. H., 1983, QJRAS, 24, 267
- Jessop N. E., Ward-Thompson D., 2000, MNRAS, 311, 63
- Jessop N. E., Ward-Thompson D., 2001, MNRAS, in press – Paper IV
- Kelsall T., et al., 1998, ApJ, 508, 44
- Kenyon S. J., Hartmann L. W., 1995, ApJSS, 101, 117
- Kessler M. F., et al., 1996, A&A, 315, L27
- Kessler M. F., Muller T. G., Arviset C., Garcia-Lario P., Prusti T., 2000, ‘The ISO Handbook Volume I: ISO – Mission Overview’, SAI/2000-035/Dc, ESA, Vilspa
- Klaas U., Haas M., Heinrichsen I., Schulz B., 1997, A&A, 325, L21
- Klaas U., Krüger H., Heinrichsen I., Heske A., Laureijs R. J., 1994, ‘ISOPHOT Observers Manual’, ESA, Noordwijk
- Lada C. J., 1987, in: IAU Symposium 115, Star Forming Regions, p. 1, eds: Peimbert M., Jugaku J., Reidel, Dordrecht
- Lada C. J., Wilking B. A., 1984, ApJ, 287, 610

- Laureijs R. J., et al., 1998, ‘ISOPHOT Data User Manual’, ISO Science Operations Centre, Villafranca
- Laureijs R. J., et al., 2001, ‘The ISO Handbook Volume V – The Imaging Photo-polarimeter’, ISO Science Operations Centre, Villafranca
- Lehtinen K., Lemke D., Mattila K., Haikala L. K., 1998, *A&A*, 333, 702
- Lemke D., et al., 1996, *A&A*, 315, L64
- Liseau R., White G. J., Larsson B., Sidher S., Olofsson G., Kaas, A., Nordh L., Caux E., Lorenzetti D., Molinari S., Nisini B., Sibille, F., 1999, *A&A*, 344, 342
- Lynds B. T., 1962, *ApJS*, 7, 1
- Mathis J. S., Mezger P. G., Panagia N., 1983, *A&A*, 128, 212
- Myers P. C., Benson P. J., 1983, *ApJ*, 266, 309
- Myers P. C., Linke R. A., Benson P. J., 1983, *ApJ*, 264, 517
- Safier P. N., McKee C. F., Stahler S. W., 1997, *ApJ*, 485, 660
- Shu F. H., Adams F. C., Lizano S., 1987, *ARA&A*, 25, 23
- Tafalla M., Mardones D., Myers P. C., Caselli P., Bachiller R., Benson P. J., 1998, *ApJ*, 504, 900
- Ward-Thompson D., 1996, *Ap&SS*, 239, 151
- Ward-Thompson D., André P., Motte F., 1998, in: Yun J. L., Liseau R., eds, ‘Star formation with the Infra-red Space Observatory’, ASP Conference Series 132, 195, San Francisco
- Ward-Thompson, D., Buckley, H.D., Greaves, J.S., Holland, W.S. & André, Ph. 1996, *MNRAS*, 281, L53
- Ward-Thompson D., Motte F., André P., 1999, *MNRAS*, 305, 143 – Paper III
- Ward-Thompson D., Scott P. F., Hills R. E., André P., 1994, *MNRAS*, 268, 276 – Paper I
- Whitworth A. P., Bhattal A. S., Francis N., Watkins S. J., 1996, *MNRAS*, 283, 1061
- Whitworth A. P., Summers D., 1985, *MNRAS* 214, 1
- Whitworth A. P., Ward-Thompson D., 2001, *ApJ*, in press
- Zhou, S., Evans, N.J. II, Koempe, C., & Walmsley, C.M. 1993, *ApJ*, 404, 232